AN ABSTRACT OF THE THESIS OF

Jordan Strahl for the degree of Master of Science in Mechanical Engineering
presented on May 20, 2022.

Title: Effect of Active Trailing Edge Motion Upon Airfoil Energy Harvester

Abstract approved: _____

James Liburdy

The application of a flapping foil with prescribed trailing edge motion to energy harvesting in a low reduced frequency ($k = fc/U_\infty$) regime was experimentally studied. The effects of the phase and amplitude of the applied trailing edge motion upon time-variant power extraction capability have been measured and are interpreted. On these bases, an optimized motion profile is developed. The airfoil design used was NACA0015 in profile with a chord length of $c = 150mm$, the pitching axis located at the 1/3 chord position, and an actively-controlled trailing edge flap hinged at the 2/3 chord location. The pitching and heaving amplitudes are $\theta_0 = 70°$ and $h_0 = 0.6c$ respectively, with a phase delay of 90°. Although the aspect ratio was 2, end plates were used to minimize 3-dimensional effects and simulate a 2-dimensional airfoil. Data were collected in a low-speed wind tunnel with turbulence intensities below 2%. The Reynolds number ($Re_c = U_\infty c/\nu$) range was $27,000 \leq Re_c \leq 60,000$ with a corresponding reduced frequency range of $0.04 \leq k \leq 0.10$. The proposed trailing edge motion profile offers a measured maximum increase of 25.6% in cycle-averaged heaving power coefficient over a rigid

foil operating under the same conditions. Results indicate that smaller trailing edge amplitudes offer greater improvements, and demonstrate that the influence of trailing edge motion can be more pronounced at low reduced frequencies.

Effect of Active Trailing Edge Motion Upon Airfoil Energy Harvester

by

Jordan Strahl

A THESIS

submitted to

Oregon State University

in partial fulfillment of
the requirements for the
degree of

Master of Science

Presented May 20, 2022
Commencement June 2022

Master of Science thesis of Jordan Strahl presented on May 20, 2022.

APPROVED:

Major Professor, representing Mechanical Engineering

Head of the School of Mechanical, Industrial, and Manufacturing Engineering

---

Dean of the Graduate School

I understand that my thesis will become part of the permanent collection of Oregon State University libraries. My signature below authorizes release of my thesis to any reader upon request.

Jordan Strahl, Author

ACKNOWLEDGEMENTS

First and foremost, I would like to thank Dr. Jim Liburdy for being an absolutely phenomenal advisor. Your guidance, mentorship, and patience have influenced my perspective for life and truly helped me grow, both professionally and in my personal life. I am forever grateful to you for the opportunities you have allotted me, both directly and indirectly.

I would further like to express my thanks to Dr. Deborah Pence for being nothing short of perfect to TA under during my first year of graduate school, as well as being a member of my committee. Over the course of the last several years, you have personally helped make it possible for me to succeed. Further thanks go out to Dr. Brian Fronk and Dr. Eric Skyllingstad for their input and commitment to being on my committee.

My work is a singular development within a long-term project. Therefore, I am very much grateful for those responsible for the accomplishments prior to and concurrent with mine. Without your efforts, this work would not have been probable.

While I had much indirect assistance from former students, I would like to express gratitude for those who helped me personally. Prominently, this includes Vickie Ngo and Kiana Kamrani for many collaborative efforts, inclusive of those during my undergraduate studies upon which this work is built. Your teamwork and willingness to lend your experiences were invaluable. Further, the generosity of Mike Prier is unparalleled. His willingness to share his time even beyond graduation was above and beyond. I would like to thank Gleb Sazanov for lending his valuable time and immense manufacturing experience. Without him, existing build quality simply

would not have been realistic. I would finally like to thank Ivan Nepomnyashchikh for many insightful discussions, as well as constant willingness to assist with many three-handed jobs without any level of obligation to this project. Your kindness and work-ethic are genuinely something else. I'm grateful for the opportunity to work with and learn from such great people.

I would like to thank my brother, Jacob Strahl, for being a welcome distraction to preserve my sanity and for his patience. Thank you for holding encoders in place while I soldered them, and especially for not freaking out that time I accidentally burned your finger.

Finally, I would like to thank my parents, Trina and David Strahl. Thank you for spending nearly two and a half decades (and counting) being my greatest sources of guidance and support in every sense. You have always been there for me while expecting absolutely nothing in return and are responsible for many of the building blocks for the foundation of my life.

TABLE OF CONTENTS

LIST OF FIGURES

LIST OF FIGURES (Continued)

LIST OF FIGURES (Continued)

Figure Page

Chapter 1: Introduction

1.1 Literature Review

Present societal needs result in a strong dependence upon electric power at a global level. Enhanced population levels coupled with technological advances present unprecedented energy demands. In order to meet power needs, focus is often shifted to reliance upon energy sources with adverse environmental effects, such as carbon-based fuels. Common examples of these power sources include the combustion of coal and gasoline. While these sources offer high energy densities, their usage results in the undesirable emission of harmful chemicals. Namely, carbon dioxide. However, further examples include atmospheric pollutants such as NOx and carbon monoxide.

Thankfully, these unfavorable effects can be prevented by shifting grid reliance to carbon-neutral sources. Many environmentally-responsible methods of collecting energy are viable. While one common example is wind farms, which are known to result in adverse environmental impacts unrelated to the generation of pollutants resulting from the usage of carbon-based fuels, such as collision-related bird deaths [1], the harvesting of kinetic energy from a fluid medium can be performed efficiently and responsibly by utilizing a lesser-known device, the airfoil energy harvester.

In the context of energy harvesting, oscillating airfoil energy harvesters were first proposed in 1981 [2]. However, the study of flapping foils is of interest in other contexts and existing literature is extensive, with related publication rates skyrocketing during the 21st century [3]. In an energy harvesting regime, the motion

of flapping foils reduces the velocity of a flow medium and converts the kinetic energy of the fluid to usable electricity. This approach to greener power has been shown to be highly efficient, with devices employing simple airfoil geometries able to operate at efficiencies between 20% and 30% [4–8]. However, it has been demonstrated that more complex airfoil geometries can further improve performance, and previous studies have investigated the influence of flexible airfoil geometries, the consequences of attached sprung tails, and the impacts of deformable leading and trailing edges [9–19].

Of the aforementioned modifications, a significant amount of study has been devoted to foil leading edge motion. Leading edge motion studies can largely be divided into two categories: passive and active approaches. Common passive approaches include leading edge motion driven by a sprung hinge, as well as foils with flexibility inclusive of the leading edge. In these designs, leading edge actuation occurs in response to exerted forces. They are the simpler of the two in design, and do not require any input signals or electrical systems. In contrast, active motions often require the usage of a motor or actuator. The motion of the electrical system of choice dictates the leading edge deflection. Typically, periodic motion is employed with a period matching that of the pitching and heaving motions. Previous studies have investigated both active and passive leading edge modifications [9–13].

Totpal and Siala explored the impact of passive, sprung leading edges upon performance characteristics [9, 11], with the results of Siala demonstrating that an increase in energy harvesting efficiency of up to 16.7% can be had via implementation of these designs [9]. Further research has been performed by Rival, who quantified influence of varied leading edge geometry upon energy harvesting performance [12], as well as Prier, who performed both numerical and experimental

investigation to characterize the capabilities of actively-controlled leading edge motion [10]. The results of Prier conclude that properly selected active leading edge motion parameters can yield an energy harvesting efficiency increase of up to 25% above that of rigid foils operating under the same conditions within the parameter ranges studied [10]. Further numerical studies regarding leading edge motion include those of Tian [5], in which numerical modeling of a foil consisting of a rigid plate with flexible leading segment was performed. The investigators were able to obtain a 1% increase in power coefficient over that of a fully-rigid plate operating under the same conditions. However, switching to active leading edge motion proved to be a much more rewarding task, resulting instead in a much more desirable increase of 11.3%.

In contrast to leading edge motion results, for which a relatively large amount of literature is available, the impacts of implemented trailing edge motion are not as well understood or quantified for energy harvesting applications. In a study conducted by Liu, trailing edge motion was discussed [13]. However, it encompassed only a portion of the overall study, which investigated the performance of bio-inspired flexible leading and trailing edges in both sole and parallel twin wing configurations [13]. The proposed design offered an enhancement of 7.68% over comparable rigid wing designs [13]. Further numerical study has investigated Gurney flaps [18] and spring-connected tails, which are somewhat similar to passive trailing edge motion [14, 16, 17]. Spring-connected tails are similar to mechanical systems evaluated for the leading edge. Current results indicate the potential to offer up to a 7.24% increase in energy harvesting efficiency relative to tailless rigid foils [15, 17]. Experimentally, the vortex dynamics of trailing edge flaps have been studied [19], and the performance of passive trailing edges employing sprung

hinges quantified [9]. In a study by Siala, sprung trailing edges offered a maximum increase in energy harvesting efficiency of 25% when compared to a baseline rigid case [9]. This measured improvement is much more substantial than existing results for spring connected tails and is indicative of sprung trailing edges offering greater performance enhancement over spring-connected tails [9, 15, 17].

Upon review of existing results for flapping foils with leading edge motion undergoing an energy harvesting regime, it is clear from existing understanding that actively-controlled components can offer greater improvements than passive components [9, 10]. Furthermore, comparing improvements obtained via implemented leading edge motion to those had via comparable trailing edge motion concludes that passive trailing edge motion improvements can offer superior increases in performance metrics than passive leading edge motions may be able to [9, 14, 17]. With both of these conclusions in mind, it is reasonable to believe that, based on available data, active trailing edge motion may offer the most substantial device improvements of all cases. Further, to the best of the author's knowledge, there are no published examples of the influence of actively-controlled trailing edge motion upon the performance of flapping foils undergoing an energy harvesting regime. This currently missed opportunity provides the basis for this work.

1.2 Problem Statement

The work presented here offers to improve understanding of airfoils undergoing a kinetic energy harvesting regime by filling the gap in literature discussed previously. Although existing works offer fantastic understanding of the influence of passive trailing edge motion, the novel use of active motion evaluated here offers

the potential to lead more in-depth discussions of vortex dynamics, inclusive of consequences of trailing edge motion phase relative to those of pitching and heaving. It is hypothesized that proper implementation of active trailing edge motion will allow influence to be imposed upon vortex shedding occurring during cyclic pitching and heaving motions. Careful selection of proper trailing edge motion timing offers the opportunity to optimize both the vortex strength and shedding time, thereby allowing further exploitation of the favorable pressure gradient induced as a result. By utilizing an airfoil design with a fitted trailing edge motor and supplied trapezoidal waveform, an experimental approach is undertaken to recognize the influence of trailing edge actuation timing relative to prescribed sinusoidal pitching and heaving motions upon the power extraction and energy harvesting efficiency of an airfoil energy harvester.

Chapter 2: Background and Parameters

2.1 Kinematic Motion

In order to achieve a kinetic energy harvesting regime, periodic motion is prescribed. The period of motion defines an individual cycle time, and a favorable pressure gradient is induced by consistent vortex shedding. In the present study, the pitching and heaving motions are both sinusoidal. The pitching motion leads the heaving motion by a prescribed phase shift, ϕ. The mathematical descriptions of these motions are:

$$\begin{aligned} h(t) &= h_0 \cos(2\pi f t) \\ \theta(t) &= \theta_0 \cos(2\pi f t + \phi) \end{aligned} \tag{2.1}$$

where f is the frequency of oscillation in Hertz and h_0 and θ_0 denote the heaving and pitching amplitudes, respectively. Trailing edge motion, however, is enforced differently. In contrast to the sinusoidal pitching and heaving motions, a trapezoidal waveform was applied to the trailing edge motor encapsulated in the airfoil used. It is hypothesized that this waveform may allow the foil to enjoy preferential cambered effects during each half-cycle. Using a program authored in LabVEIW 2013, the amplitude and phase of the waveform relative to the pitching and heaving oscillations can be adjusted. In the first portion of the study, an amplitude of 40° was utilized for all four motions considered. Figure 2.1 visualizes all trailing edge motions for this case. In the second portion of the study, two waveforms of interest were selected from the initial portion and considered again at an amplitude

of 20°. Figure 2.2 shows the reduced amplitude motions. As a consequence of the employed hinged mechanism located at the trailing edge, small gaps must be present between components. This, coupled with trailing edge motor and gearbox friction, results in a small, inherent give in the wing in this location. Therefore, Figures 2.1 and 2.2 are not exact representations of trailing edge deflections.

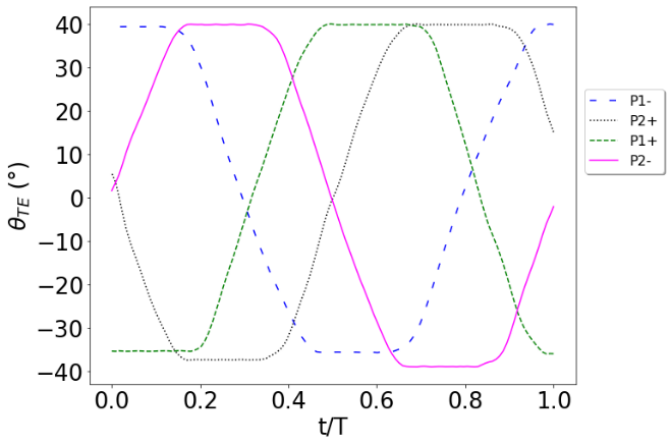

Figure 2.1: All four trailing edge motions at an enforced 40° amplitude.

In Figures 2.1 and 2.2, each motion is denoted as "P#(sign)". It is important to note that this naming convention is not an artifact of randomness. The "P" denotes the word "phase". The following number is the phase number. Two phases are considered: P1 and P2. Finally, the sign used is indicative of direction, and differentiates the positive and negative motions.

Two motions denoted by the same phase number but different signs have the same phase delay relative to the pitching and heaving actuations, but different trailing edge actuation directions. Positive motions correspond to trailing edge actuations in the direction opposing the sign of the pitching waveform, while negative motions denote trailing edge motor actuations in the same direction of the

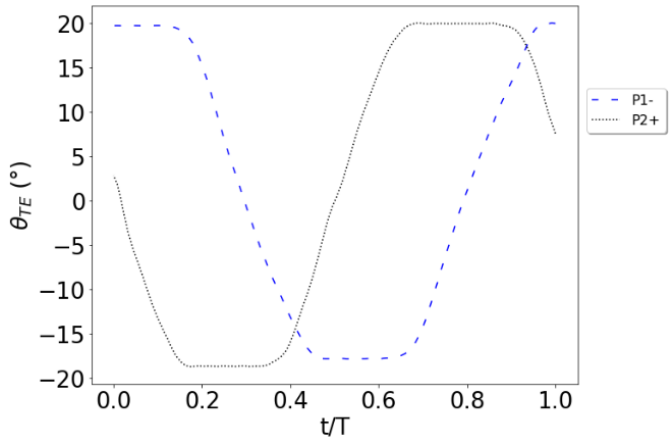

Figure 2.2: The two trailing edge motions from the initial portion of the study, adjusted to new trailing edge amplitudes of 20°.

pitching waveform. Note that this does not mean that the trailing edge is always oriented in a particular direction during the entire cycle. Rather, the articulation of the trailing edge deflection is a function of both the sign of the motion (positive or negative) applied, as well as the phase applied relative to pitching and heaving. Figure 2.3 illustrates difference between positive and negative motions.

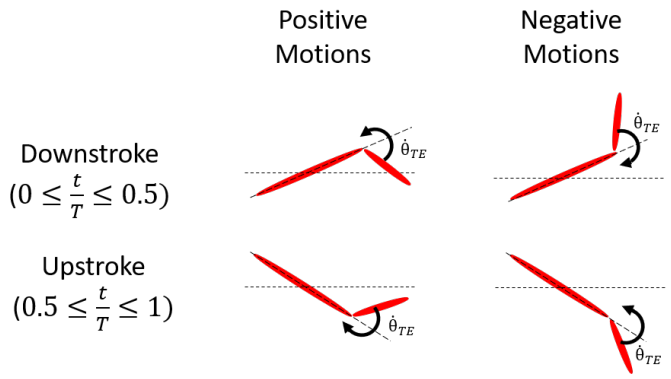

Figure 2.3: Visualization of the discrepancy between the actuation of the trailing edge motor in positive motion cases and the actuation of the trailing edge motor in negative motion cases.

The two imposed trailing edge motion phases, Phase 1 and Phase 2, in conjunction with the possible positive or negative case of each motion totals four cases. Since two motions are to be evaluated at reduced amplitudes, a total of 6 trailing edge waveforms are selected for analysis. Figures 2.1 and 2.2 together illustrate all of these motion profiles.

A key distinction between experimental cases is ratio of oscillatory time scale to the convective time scale. This parameter is defined as the reduced frequency and is described by Equation 2.2.

$$k = \frac{fc}{U_\infty} \tag{2.2}$$

In Equation 2.2, f is the frequency of oscillation in Hertz, c is the foil chord length, and U_∞ is the freestream velocity. The freestream velocity is often a key adjustment parameter when obtaining a desired reduced frequency, and its value directly influences the magnitude of the lift forces experienced by the airfoil. Once the lift forces are known, all parameters of interest in the study can be computed from them. Since these forces are directly measured during the experiment, the transient coefficient of lift (given by Equation 2.3) can be readily obtained in post-processing.

$$C_L = \frac{F_L}{\frac{1}{2}\rho U_\infty^2 cs} \tag{2.3}$$

In the above, F_L is the measured lift force after moment corrections and filtering are applied. The density of the freestream fluid is denoted as ρ, c is the foil chord length, and s is the foil span. The instantaneous heaving power output of the energy harvester can also be computed directly from the measured lift forces. Equation

2.4 defines the total instantaneous power output of the device.

$$P(t) = F_L(t)\dot{h}(t) + M(t)\dot{\theta}(t) \tag{2.4}$$

The total instantaneous power output is denoted as P(t). The transient lift forces are denoted by $F_L(t)$, while $\dot{h}(t)$ is the heaving velocity, M(t) is the moment, and $\dot{\theta}(t)$ is the pitching velocity. The first term on the right-hand side is the heaving contribution to instantaneous power extraction, while the second term on the right-hand side is the pitching contribution. However, it has been shown that, at low reduced frequencies, pitching contributions are often negligible relative to heaving contributions, which dominate power extraction [4]. With this in mind, the present study is concerned only with the heaving component of instantaneous power. Equation 2.4 therefore simplifies to Equation 2.5.

$$P(t) = F_L(t)\dot{h}(t) \tag{2.5}$$

With the transient power extraction known, the cycle averaged power can be computed according to Equation 2.6.

$$\bar{P} = \frac{1}{T}\int_t^{t+T} P(t)dt \tag{2.6}$$

In Equation 2.6, T denotes the period of the energy harvesting cycle. By further utilizing the transient heaving power extraction, the transient heaving power coefficient may also be computed, according to Equation 2.7.

$$C_P = \frac{P(t)}{\frac{1}{2}\rho U_\infty^3 sc} \tag{2.7}$$

2.2 Performance Metrics

While the previous section introduces some characteristics of results, measurements will predominately be compared on a basis of the energy extraction efficiency, η, and the cycle-averaged heaving power coefficient, $\bar{c_p}$, to contrast individual device enhancements.

After calculating all values described in the previous section, the cycle-averaged heaving power coefficient may be computed directly via Equation 2.8 by utilizing the cycle averaged heaving power extraction. Comparing Equations 2.7 and 2.8, it is mathematically clear that this is simply a time-averaged representation of the transient heaving power coefficient.

$$\bar{C_P} = \frac{\bar{P}}{\frac{1}{2}\rho U_\infty^3 sc} \tag{2.8}$$

The second key performance metric, the energy extraction efficiency, can also be obtained.

$$\eta = \frac{\bar{P}}{P_S} = \frac{\bar{P}}{\frac{1}{2}\rho U_\infty^3 bd} \tag{2.9}$$

In Equation 2.9, two new parameters are introduced: P_S, and d. P_S is the power supplied by the fluid through the area swept by kinetic motion of the airfoil. This is the product of the foil span and the length swept by the foil's flapping motion, d. Due to the phase delay (ϕ) between the pitching and heaving motions, d is not simply equal to twice the heaving amplitude (h_0). Rather, it is a function of the maximum tail deflection. As a consequence of the varied trailing edge phase delay and trailing edge amplitudes, different motions will have different values of d as functions of when the trailing edge actuates, in which direction movement occurs,

and upon the trailing edge amplitude in each particular case. For P1- motions, the swept area is increased. In P1+ cases, the swept area is reduced. Both P2- and P2+ are approximately unaffected by this effect as illustrated in Figure 2.1. For lower trailing edge amplitudes, this effect is less pronounced.

Therefore, while efficiency is a critical measure of success, the cycle averaged coefficient of heaving power remains important to contrast the influence of trailing edge motions given that it is not a function of the swept area. For practical reasons, this may make the latter a more crucial consideration in some cases. With this in mind, both are calculated, presented, and discussed.

2.3 Experimental Conditions

In the present study, reduced frequencies of $k = 0.04,\ 0.06,\ 0.08$, and 0.10 are considered. For the lowest three reduced frequencies, an oscillation frequency of 1.6 Hz is used. However, for cases with $k = 0.10$, the oscillation frequency was increased to 1.8 Hz. With a foil chord length of 0.15 m, the corresponding Reynolds number range is $27,000 \leq Re_c \leq 60,000$. A phase delay of $\phi = 90°$ is used to separate the pitching and heaving cycles, which occur with amplitudes of $\theta_0 = 70°$ and $h_0 = 0.6c$ respectively. The pitching axis is located at the third-chord, with the trailing edge flap hinged 2c/3 from the leading edge.

Initially, all four trailing edge motions (P1+, P1-, P2+, and P2-) are considered at a trailing edge amplitude of 40° and reduced frequency of $k = 0.08$. These trailing edge motions are illustrated in Figure 2.1. Based on the results, two trailing edge motions are deemed promising on a basis of energy extraction efficiency (η) and cycle averaged heaving power coefficient ($\bar{C_P}$). These motions are then studied

again under the same conditions, but with a reduced trailing edge amplitude of 20°. Combining these results with those obtained initially allows selection of two preferred experimental cases of the 6 studied, which are then further examined under reduced frequencies of $k = 0.04,\ 0.06$, and 0.10.

Chapter 3: Methodology

3.1 Experimental Facility

Experiments were conducted in a closed-loop, recirculating wind tunnel with a test section size of 1.37m x 1.52m and turbulence intensities below 2%. Freestream airflow is delivered by motorized rotation of a Hartzell propeller. Altering the propeller rotation rate allows the wind speed, measured directly using a FlowKinetics FKT 3DP1A manometer in conjunction with a Pitot tube situated upstream of the foil, to be adjusted. The apparatus is situated on the downstream side of the propeller to maximize flow stability.

3.2 Airfoil

The foil selected for investigation is a NACA0015 airfoil, which performs well in an energy harvesting regime [20, 21]. By convention, NACA00XX series foils have a maximum thickness of XX% of the foil's chord length. Their profile is mathematically-driven according to Equation 3.1:

$$y = 5t * \left(0.29690x^{\frac{1}{2}} - 0.12600x - 0.35160x^2 + 0.28430x^3 - 0.10150x^4\right) \quad (3.1)$$

where y denotes the profile about the mean camber line and t is the thickness as a fraction of the chord [22]. For a NACA0015 airfoil, the maximum thickness is

15% of the chord length, and thus $t = 0.15$. The foil's pitching axis is located at the third-chord. This parameter has also been shown to enhance energy harvesting efficiency [20, 23, 24]. The foil used has a chord length of $c = 150mm$ and span of $s = 300mm$. The aspect ratio (the ratio of the span to the chord length) is therefore 2. It has been shown that below an aspect ratio of 4, 3-dimensional effects dominate [25]. Therefore, endplates were used to simulate a 2-dimensional system.

The foil used was designed and manufactured in-house. The airfoil body used consists of 3D printed acrylonitrile butadiene styrene (ABS) plastic components, which are otherwise hollow in order to minimize mass and therefore inertial forces associated with flapping motion. This is critical, given that inertial forces associated with the foil's flapping motion have been shown to be substantial when the freestream fluid is air [26]. Minimizing the inertial forces can therefore help reduce experimental uncertainty. A small stainless steel component is used in the trailing edge body to mate with the trailing edge motor shaft. This component has very tight tolerances in order to minimize slop in the mate between the trailing edge motor and trailing edge. In addition to the need for very precise manufacturing, this component further must be made of metal in order to prevent stress cracking. The only other manufactured metal component used is the pitching axis rod, which is made from 7075 high-strength aluminum. The rod is epoxied internally along the foil span and mates the foil body to the pitching and heaving apparatus, which will be discussed in detail later on. Trailing edge motion was accomplished using a motor integrated into the wing design. The motor is situated 2c/3 downstream of the leading edge and actuates the trailing edge, defined as the remainder of the foil downstream of the trailing edge motor, relative to the main body. The integrated trailing edge motor used in the airfoil is a brushed DC Micro Metal

Gearmotor HPCB 12V with an attached 150:1 ratio gearbox. The motor is fitted with a magnetic encoder which reports the motor shaft position with a precision of $\pm 0.2°$. A program authored in LabVIEW 2013 interfaces with the motor and supplies a trapezoidal waveform with variable amplitude and phase. At the interface between the trailing edge and the main body, a cammed hinge design is employed to minimize flow through the wing. Figure 3.1 shows the foil design CAD model. Figure 3.2 illustrates the hinge design.

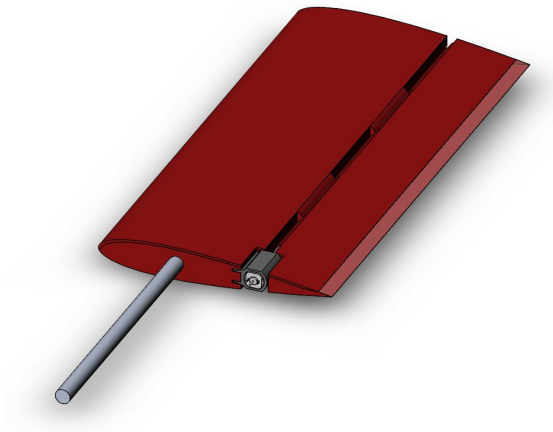

Figure 3.1: CAD model of in-house manufactured airfoil used in the present study.

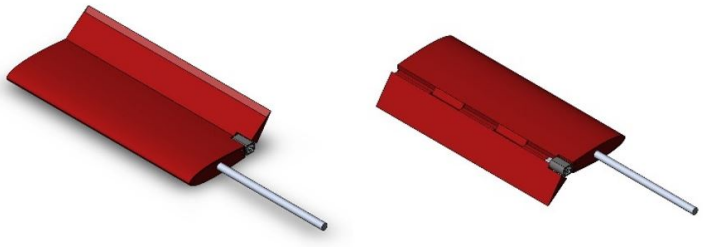

Figure 3.2: Cammed hinge design used to minimize flow between the airfoil body and trailing edge components.

Although the main body was 3D printed in order to minimize mass, the two metal components used each required light machining. The rod used for the pitching axis was cut to length and two flat surfaces ground. These were used as mates to the main foil body, ensuring that no unwanted rotation about the pitching axis would occur. The trailing edge motor shaft mate was milled to rough dimensions and finished via WireDM. This was required, given the curvature required in order to properly mate with the cammed 3D printed trailing edge hinge. Components were then assembled and affixed via Gorilla Glue brand epoxy. Upon completion of final assembly, the foil body was sanded for smoothness, primed, and painted matte black in color. This was done to improve contrast for future flow visualization and particle image velocimetry (PIV) studies. The manufacturing process is documented in Figures 3.3, 3.4, and 3.5. The completed foil is installed in the experimental apparatus in Figure 3.6.

Figure 3.3: Airfoil with pitching rod epoxy curing inside of main body. Also shown are the other foil components, yet to be assembled.

Figure 3.4: Airfoil with installed pitching rod and partially assembled components. Only the top covers for the trailing edge and main body are left to be installed.

Figure 3.5: Completed airfoil after assembly, curing of epoxy, sanding, and application of primer and paint.

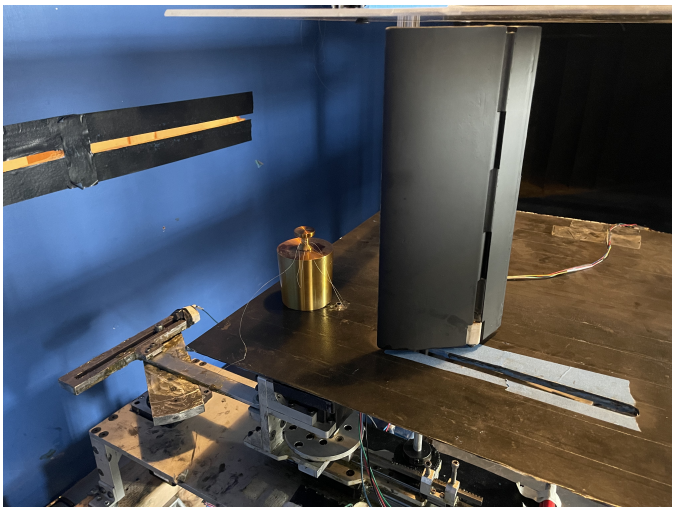

Figure 3.6: Manufactured airfoil affixed in experimental apparatus inside of wind tunnel.

3.3 Pitching and Heaving Apparatus

Foil flapping motion was accomplished by an in-house built pitching and heaving apparatus controlled using a National Instruments system consisting of LabVIEW 2013, a BNC-2110, and a PCI-6221. This allows interface with device electrical systems. The pitching and heaving motor controllers, both of which are Gecko Drive G203V Vampire digital stepper motor drivers, are connected to Gecko Drive stepper motors (G734-1280-4 and G723-400-4 for pitching and heaving respectively) and feature custom 2000:1 windings by Lin Engineering to achieve the desired flapping motion frequency. The larger heaving motor is affixed to a Scotch yoke mechanism and moves the pitching carriage, causing heaving motion. The smaller pitching motor is situated in a rack-and-pinion system and drives foil pitching motion. The foil is situated vertically in order to isolate flapping motion inertial forces from gravitational effects. Figure 3.7 shows the mechanical apparatus model. The

installed airfoil and endplates are shown in Figures 3.6 and 3.8. Endplates are situated approximately 4mm from the ends of the airfoil to minimize 3-dimensional effects and simulate a much longer aspect ratio.

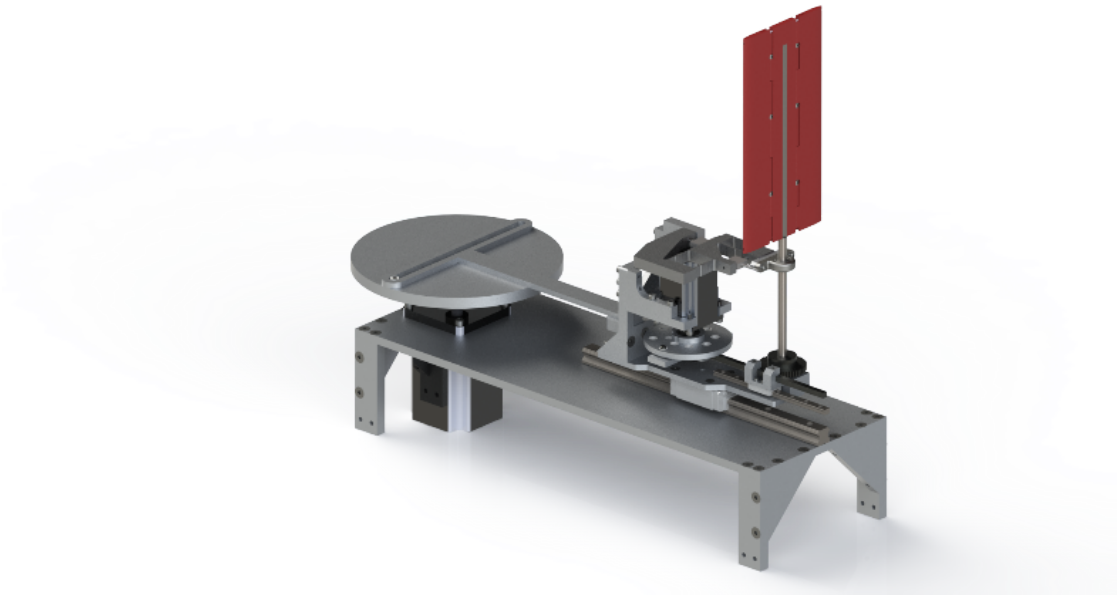

Figure 3.7: Pitching and heaving apparatus model. Adapted from [26].

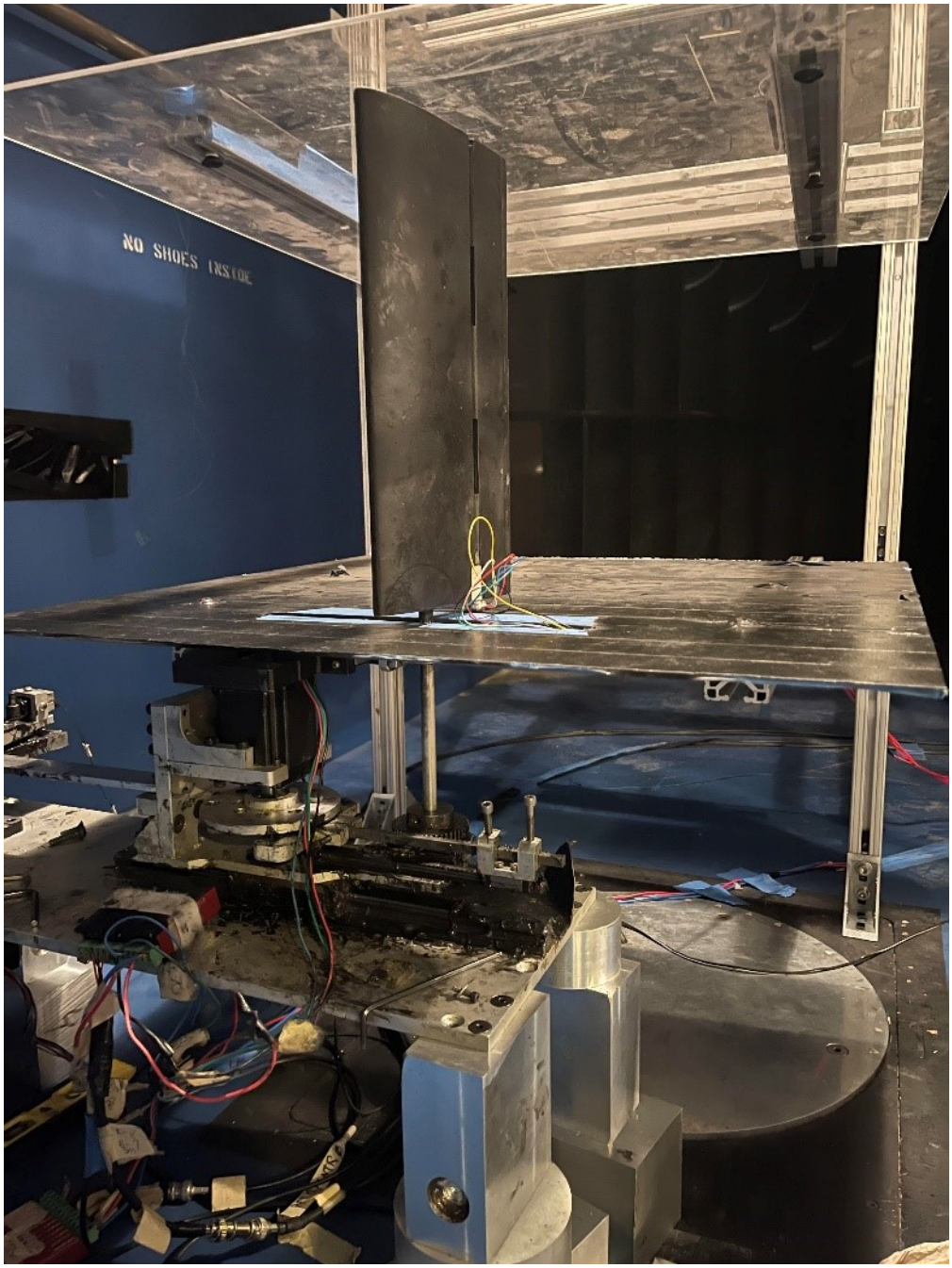

Figure 3.8: Completed airfoil installed with accompanying endplates.

3.4 Force Measurement Techniques

Direct force measurements were taken using Futek LSB200 load cells. Load cell signals were fed through an in-house built amplifier before reaching the BNC-2110 and being read by LabVIEW. Since the angle of attack is unsteady, force measurements must be along multiple axes in order to fully describe aerodynamic loads throughout the cycle. Load cells were therefore situated in a housing to minimize crosstalk. The housing is shown in Figure 3.9.

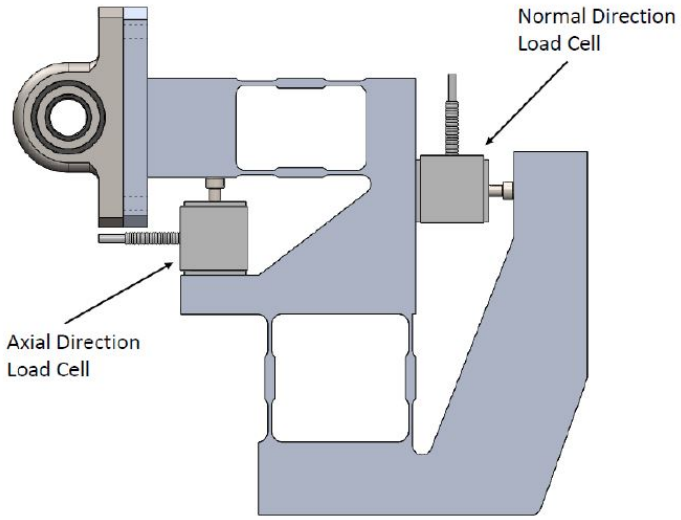

Figure 3.9: Load cell fixture employed to reduce crosstalk.

To further prevent crosstalk, force calibrations were performed prior to experiments. This process is detailed by Totpal in [26]. Briefly stated, load cells are pretensioned and measurements taken. A known mass is then applied in each direction of interest (along the chord and normal to the foil body). Using Newton's equation ($\Sigma F = ma$) in conjunction with the known acceleration due to gravity, the force applied by the mass upon the cell can be computed. This, in conjunction

with the measurements taken, allows propagation of Equation 3.2:

$$\begin{vmatrix} F_N \\ F_A \end{vmatrix} = \begin{vmatrix} M_{V_N \ on \ F_N} & M_{V_A \ on \ F_N} \\ M_{V_N \ on \ F_A} & M_{V_A \ on \ F_A} \end{vmatrix} \begin{vmatrix} V_N - V_{N,0} \\ V_A - V_{A,0} \end{vmatrix} \tag{3.2}$$

where F_N is the force in the normal direction, F_A is the force in the axial direction, V_N is the voltage reading from the load cell oriented in the normal direction under application of the known mass in the normal direction, V_A is the voltage reading from the load cell oriented in the axial direction under application of the known mass in the axial direction, $V_{A,0}$ is the voltage reading from the load cell oriented in the axial direction under application of no load, and $V_{N,0}$ is the voltage reading from the load cell oriented in the normal direction under application of no load. Upon completion of calibration prior to experiments, force measurements were taken at 200 Hz at the location of the bearing connecting the foil pitching rod to the load cell housing. Since the equivalent aerodynamic point load occurs at the midpoint of the span, a torque correction factor must be applied to measured values. This was done in post-processing according to Equation 3.3:

$$F_{aero} = \frac{F_{LC} L_{LC}}{L_{aero}} \tag{3.3}$$

Where F_{aero} is the aerodynamic load exerted on the foil by the fluid, F_{LC} is the force measured by the load cells, L_{LC} is the vertical distance from the load cell measurement point to the base of the pitching rod, and L_{aero} is the vertical distance from the midpoint of the foil span to the base of the pitching rod.

3.5 Data Acquisition

Experiments began with the wind tunnel propeller and all actuation motors turned off. The pitching, heaving, and trailing edge motors are then all manually set to known datum angles before they are supplied power. The midpoint of the upstroke is used as the starting point. This defines the set point of the heaving motor. The pitching motor and trailing edge motor are each set to 0°. Motor power supplies are turned on and the phase delay between the pitching and heaving motions, ϕ, is enforced by LabVIEW. The pitching and heaving frequency, f, and trailing edge waveform parameters are set in LabVIEW and applied. The device is then allowed to run freely for 45 seconds. This time is used by the operator to ensure that all systems are behaving normally, and also serves to allow mechanical vibrations to develop to steady-state. Upon completion of this final set-up step, the actual experiment begins and force reading recording begins.

It has been shown that foil inertial forces associated with flapping motion are substantial when the freestream medium is air [26]. Therefore, the first period of each test case is conducted with an applied wind speed of 0 m/s in order to isolate inertial forces. A time of 60 seconds is allotted for this. During this time period, around 100 cycles occur. These will be statistically analyzed and collapsed into a single inertial cycle in post-processing. The desired wind speed is then applied via the wind tunnel propeller. However, this process is not immediate and flow boundaries must be allowed to develop. Another 60 second period is allotted for this process. Therefore, although the device is already actively running and collecting data, data during the second minute of the experiment is immediately discarded as a first order of business during post-processing. The final 60 seconds of experiment entails the collection of combined inertial and lift forces. With the device still

running, inertial force data collected, and flow boundaries developed, useful data pertaining to aerodynamic loads may be collected. The data collected during this final period is also to be statistically analyzed and collapsed into a single inertial cycle in post-processing, just as that of the inertial force data collected during the first minute of data collection. Upon completion of this final experimental portion, the airfoil and propeller motors are ramped down, turned off, and reset for the next run. Lubricant is applied as-needed.

3.6 Data Processing

Post-processing of data was performed in Python 3.7. Data is first interpolated in order to produce even timesteps, a feature which is not present in the existing LabVIEW software for measurements recorder as rapidly as 200 Hz. A third order Butterworth filter is then applied with a cutoff frequency of 8 Hz. This completes the initial stage of post-processing. The next step is to divide the data into individual components based upon corresponding portions of the experiment.

Since the data collected during the second minute is representative of flow-boundary development conditions, it is not physically meaningful in the context of the present study. Therefore, this data is thrown out. The remaining data is divided into 2 components: data from the first minute (representative of unsteady inertial forces), and data from the third minute (representative of unsteady inertial and lift forces). The following procedure is then performed twice, once for each component of data.

Using the digital signal supplied by a mechanical button affixed to the heaving Scotch yoke, the start and end points of individual cycles are identified. This allows

each component to be divided into individual cycles. Using all data points within all cycles, a median cycle from each component is then found. All cycles within each component are then compared to their respective median cycle, and any cycle falling outside of a standard deviation from the median cycle at any data point is removed. The resulting two data sets represent filtered versions of the initial two components. Each data set is then averaged at each data point in order to obtain an averaged cycle for both the first minute and the third minute.

Subtracting the measured isolated inertial forces from the first-minute data from the inertial + lift force data from the third minute then allows the cyclic lift forces to be isolated according to Equation 3.4:

$$F_{aero} = (F_{inertial} + F_{aero}) - F_{inertial} \tag{3.4}$$

where F_{areo} represents aerodynamic loads, $F_{inertial}$ represents inertial forces, the term $(F_{inertial} + F_{aero})$ is representative of data collected during the third minute of the experiment, and $F_{inertial}$ is representative of data collected during the first minute of the experiment. The filtered and averaged first minute cycle is therefore then subtracted from the filtered and averaged third minute cycle to obtain the isolated lift forces.

This final cycle difference is representative of the unsteady, filtered, measured aerodynamic force data. However, it is still in the form of the the uncorrected measurements taken at the location of the load cells. These forces are not the equivalent point load lift forces. Therefore, the moment correction given in Equation 3.3 is then applied to determine the lift forces from the measured forces. From this, the coefficient of lift can be directly computed. However, the coefficient of power requires slightly more effort to obtain. Since the prescribed heaving motion

is sinusoidal, the frequency of the obtained lift force curve is used to model the prescribed heaving velocity. This allows calculation of the power output as a function of time, allowing the unsteady coefficient of power to be obtained. The cycle averaged power is obtained using a numerical integral, and the swept area computed by utilizing the maximum foil position perpendicular to the flow. This allows the efficiency and cycle averaged power coefficient, which both serve as key performance metrics, to be calculated.

3.7 Experimental Uncertainty

Because the first and third minute measurements are processed individually, each data set has its own standard deviation at each time step. These two standard deviation sets are described by Equation 3.5.

$$\sigma = \sqrt{\frac{\Sigma \left(x_i - \overline{x}\right)^2}{n-1}} \tag{3.5}$$

At each time step, the uncertainty present in the coefficient of lift reported is therefore the non-dimensionalized sum of the uncertainty in the filtered first minute data and the filtered third minute data. This is given by Equation 3.6.

$$\sigma_{CL} = \frac{\sigma_{inertial} + \sigma_{inertial+lift}}{\frac{1}{2}\rho U_\infty^2 cs} \tag{3.6}$$

Figure 3.10 shows the measurement uncertainty in the first and third minute data for the rigid test case at a reduced frequency of $k = 0.08$, obtained using Equation 3.5. Figure 3.11 shows the experimental uncertainty in the transient coefficient of lift corresponding to the data shown in Figure 3.10 obtained using

Equation 3.6. The pitching and heaving apparatus used in the present study has been designed and calibrated to reduce uncertainties, which are similar to those reported by Ngo in [27] under similar conditions with the same device.

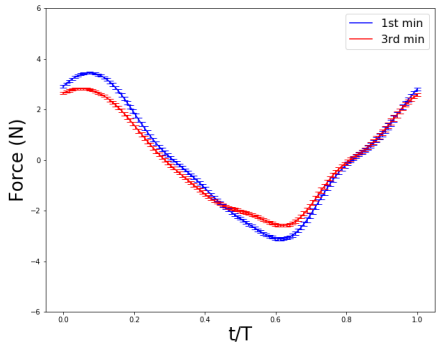

Figure 3.10: Measurement uncertainty in the first and third minute data for the rigid test case at a reduced frequency of $k = 0.08$, obtained using Equation 3.5.

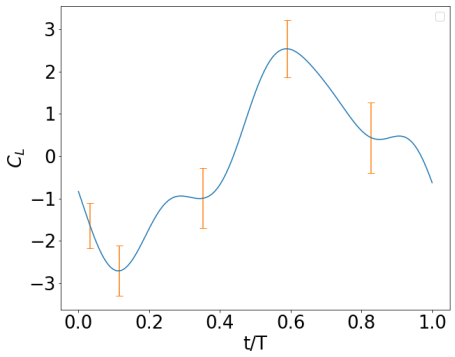

Figure 3.11: Experimental uncertainty in the transient coefficient of lift corresponding to the data shown in Figure 3.10 obtained using Equation 3.6.

Chapter 4: Results & Discussion

4.1 Effect of Trailing Edge Waveform Phase

The first parameter of interest is the optimization of the trailing edge waveform phase. It is hypothesized that, just as an idealized phase delay between pitching and heaving of 90° has been identified by numerous previous studies, an idealized phase selection for trailing edge motion may also exist. Positive and negative cases of each trailing edge motion phase were therefore investigated at a reduced frequency of $k = 0.08$ and trailing edge amplitudes of 40°. The transient coefficient of lift for each waveform shown in Figure 2.1 and a rigid case taken with the same airfoil are given in Figure 4.1. The corresponding transient coefficients of heaving power are given in Figure 4.3, and the calculated efficiencies and cycle mean coefficients of heaving power are compared in Figures 4.2 and 4.4 respectively. Although the enforced kinematic motion parameters are symmetric for each half of the cycle, exact measurements demonstrate some deviation between behavior during the first and second halves of the cycle. Consequentially, full-cycle results are not entirely consistent with those computed on a half-cycle basis.

The P1- test case demonstrates the most immediately-clear impact upon performance relative to the rigid case. As illustrated in Figure 4.1, it has a greater maximum lift force occurring at approximately the same cycle times. Further, the secondary peak is accentuated. However, forces between the two peaks are reduced. Heaving velocity is maximized at the midpoint of each half-cycle. Therefore, the reduction in forces relative to the rigid case occurs with very unfortunate timing.

Consequentially, an 8.3% reduction in the cycle-mean heaving power coefficient, $\bar{C_p}$, is observed. Due to the nature of the motion, the efficiency is further reduced due to an increase in the swept area. A reduction of 17.4% is observed compared to the rigid case results.

The corresponding positive motion, P1+, is the second least desirable performer of the group with respect to power extraction. While it manages to delay both the primary and secondary peaks during the first half of the cycle, this behavior does not continue during the second half of the cycle. Further, a drastic reduction in peak force magnitudes are observed. While the primary peak during the first half of the cycle occurs at approximately $t/T = 0.22$ when heaving velocity is nearly maximized, the reduction in magnitude occurring as a consequence of trailing edge motion still prevents the peak power extraction from becoming significant. Further, this shift is not observed during the second half of the cycle. Beyond this, suppression of forces near the primary peaks results in a substantial reduction in the area under the heaving power curve, resulting in undesirable cycle mean power extraction. Although the timing of the deflection of the trailing edge causes the swept area to be reduced, the reduction in the cycle averaged heaving power coefficient is 22.3% relative to the rigid case results. This reduction in swept area is not enough to overcome this effect, resulting in a small efficiency reduction which is within experimental uncertainty relative to the rigid case.

The performance of the P2- test case is the least desirable of those explored at this stage. While it does manage to delay peak force occurrence until slightly later in the cycle relative to the rigid case, this comes at a cost of a suppressed secondary peak during the first half of the cycle. Furthermore, forces between peaks are also suppressed, substantially reducing the area under the heaving power curve

in Figure 4.3. A large negative region in the transient coefficient of power curve (see Figure 4.3) occurs, particularly at the very end of the cycle. A reduction in swept area does not occur. Therefore, the reduction in cycle mean heaving power coefficient and efficiency are the same - both are reduced by 31.6%.

Under the conditions examined in this section, P2+ is the test case which manages to come close to improving upon the results of the rigid case. This is accomplished by delaying the onset of peak lift forces at the expense of their magnitude while simultaneously increasing the magnitude of secondary peak forces. When this motion profile is implemented, lift forces occur with nearly optimal synchronization to maximum heaving velocity. Although they occur relatively late in the cycle (when heaving velocity is close to zero), the results for P2+ demonstrate the largest secondary peak force values of all test cases in this section. As a consequence, a relatively broad coefficient of power curve is measured as shown in Figure 4.3, yielding desirable performance.

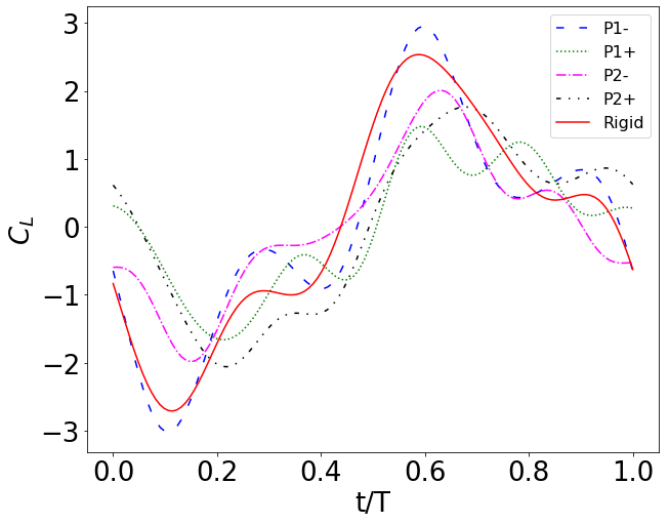

Figure 4.1: Transient coefficients of lift for positive and negative cases of both motion profiles at a trailing edge amplitude of 40° and reduced frequency k = 0.08. Also shown are rigid case results taken with the same airfoil under the same experimental conditions.

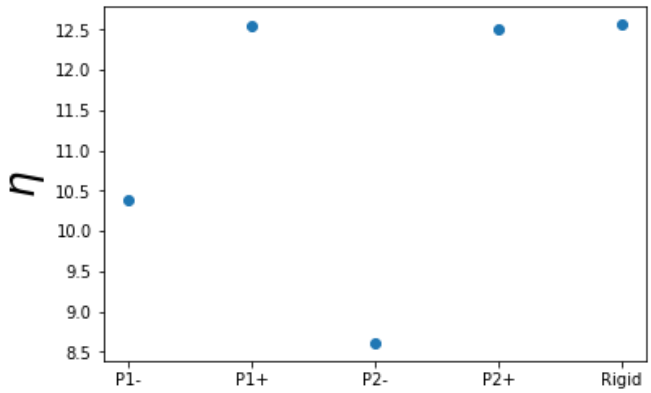

Figure 4.2: Cycle efficiency for positive and negative cases of both motion profiles at a trailing edge amplitude of 40° and reduced frequency k = 0.08 shown with datum rigid case results.

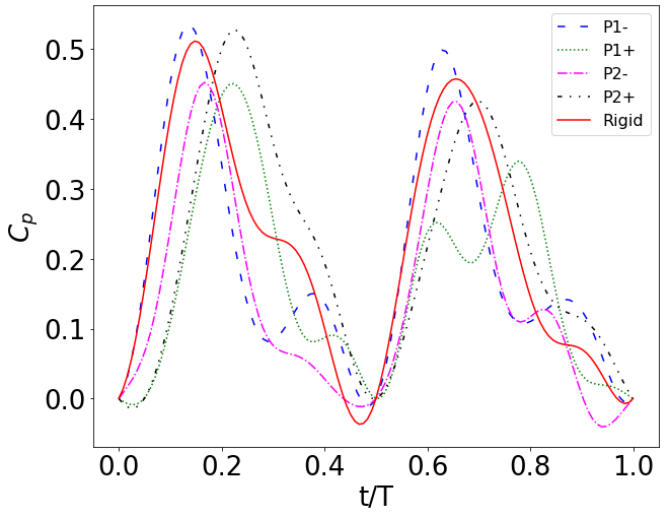

Figure 4.3: Transient coefficients of heaving power for positive and negative cases of both motion profiles at a trailing edge amplitude of 40° and reduced frequency k = 0.08. Also shown are rigid case results taken with the same airfoil under the same experimental conditions.

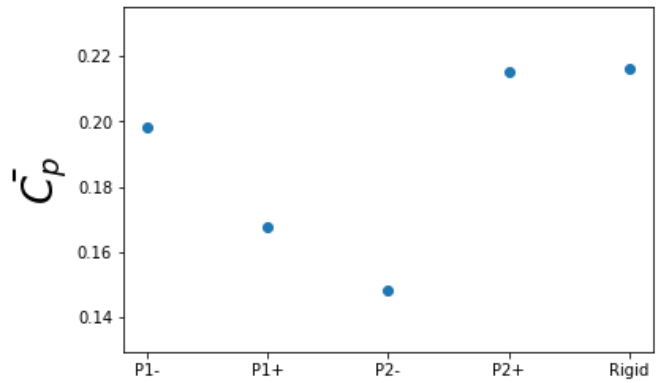

Figure 4.4: Cycle mean heaving power coefficient for positive and negative cases of both motion profiles at a trailing edge amplitude of 40° and reduced frequency k = 0.08 shown with datum rigid case results.

4.2 Effect of Trailing Edge Deflection Amplitude

The effect of the enforced trailing edge motion phase has been determined. Usage of both the P1- and P2+ motion profiles delivered promising results worthy of future investigation. Therefore, the trailing edge amplitude was reduced from 40° to 20° while a reduced frequency of k = 0.08 was maintained. The adjusted-amplitude waveforms are shown in Figure 2.2. This presents two new cases (P1- and P2+ at amplitudes of 20°) with performance characteristics which contrast interestingly to three comparable cases from the previous section (P1- and P2+ at amplitudes of 40°, as well as the baseline rigid foil results).

When the trailing edge amplitude is reduced for P1-, the result is hugely favorable. While a cycle averaged heaving power coefficient reduction of 8.3% relative to the rigid case results was observed at the greater trailing edge amplitude in the previous section, the reduced amplitude case under the same experimental conditions demonstrates a 8.8% improvement over the same baseline case. The efficiency, which was measured as a 17.4% reduction at the greater trailing edge amplitude, is improved by 1.4% over the rigid case as a consequence of the increased swept area. As a consequence of the reduction in the trailing edge amplitude, the swept area is correspondingly reduced, although it is still greater than that of the rigid case.

These improvements can be attributed to improved timing of force maxima. At the greater amplitude of 40°, P1- was able to increase peak forces at the expense of reduced force magnitudes at other times. However, at the reduced amplitude, the measured force magnitudes are nearly indistinguishable from those of the rigid case. While the secondary peak in the second half of the cycle is noticeably improved, it occurs so late in the half-cycle that its impact upon energy extraction is close to minimal. Regardless, this is not the key advantage offered. Rather, at the

reduced amplitude, P1- is able to delay larger force magnitudes until later on in the cycle relative to the rigid case with no notable adverse consequences with respect to magnitudes or otherwise. This effect is well illustrated by Figure 4.5, and its impact upon power extraction clearly seen in Figure 4.6. The area under the power curve is visibly larger than that of the rigid case results, demonstrating promising performance and a preference for lower trailing edge amplitudes on behalf of the P1- motion profile.

Further, P2+ also produces more desirable results at the lower trailing edge amplitude. While its efficiency and cycle mean heaving power coefficient were nearly indistinguishable from those of the rigid case results at the larger amplitude, reducing the amplitude produces a substantially more favorable effect, resulting in improvements of 12.0% relative to rigid case values.

These results are the consequences of lift force behavior similar to those of the P1- test case at the reduced amplitude of 20°. However, the magnitude of the primary peak occurring during the first half of the cycle is slightly increased, with its phase shift slightly reduced. The reduction in force magnitude occurring between this peak and the secondary peak becomes more drastic. In the second half of the cycle, the magnitudes of the primary peaks of the two lower amplitude trailing edge motion cases and the primary peak of the rigid case results are all three nearly identical, with one key distinction: the P1- case manages to delay the peak (as noted above), while the P2+ case manages to slightly delay it again (to even later than the primary peak of the P1- case). An improvement is also observed in the secondary peak magnitude occurring during both the first and second halves of the cycle. As a result of improved peak magnitudes and timing, P2+ manages remarkable power extraction as illustrated in Figure 4.6 and Figure 4.8. Thus far,

P2+ has been the best trailing edge motion profile performer at both amplitudes, and is now managing a greater power extraction than the rigid case.

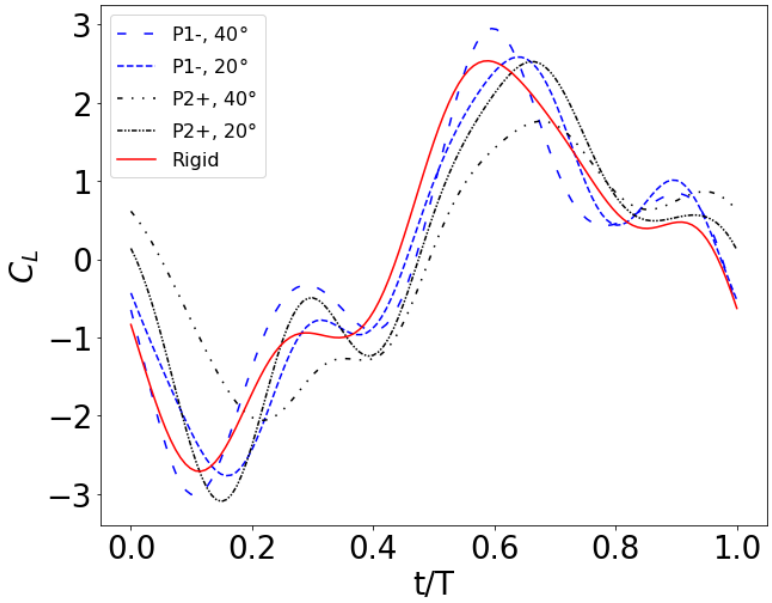

Figure 4.5: Transient coefficients of lift for P1- and P2+ trailing edge motions at trailing edge amplitudes of 40° and 20° with reduced frequency k = 0.08. Also shown are rigid case results taken with the same airfoil under the same experimental conditions.

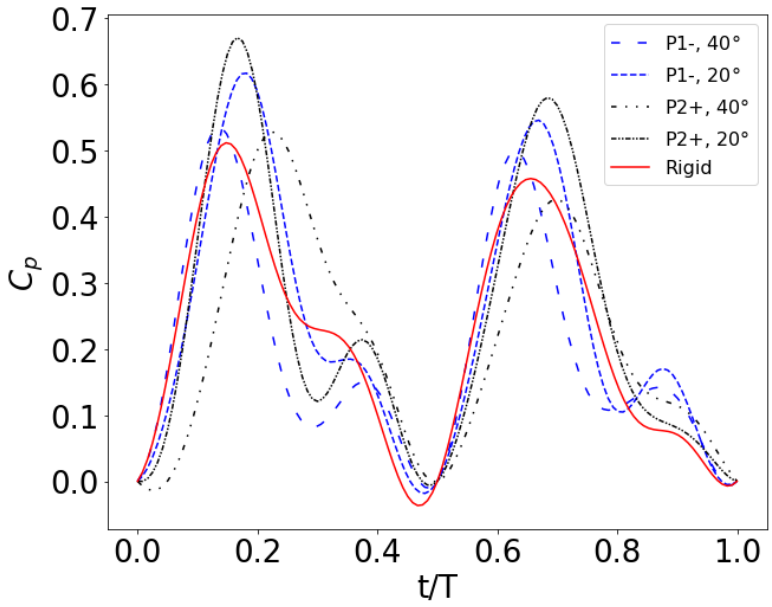

Figure 4.6: Transient coefficients of heaving power for P1- and P2+ trailing edge motions at trailing edge amplitudes of 40° and 20° with reduced frequency k = 0.08. Also shown are rigid case results taken with the same airfoil under the same experimental conditions.

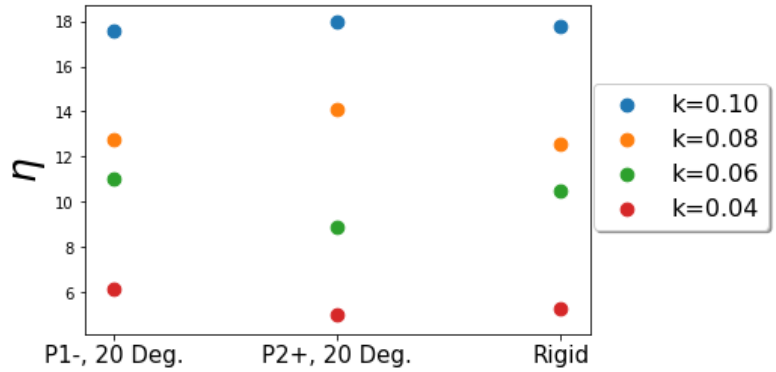

Figure 4.7: Cycle efficiency for rigid case and P1- and P2+ trailing edge motions at a trailing edge amplitude of 20° with reduced frequency k = 0.10, 0.08, 0.06, and 0.04.

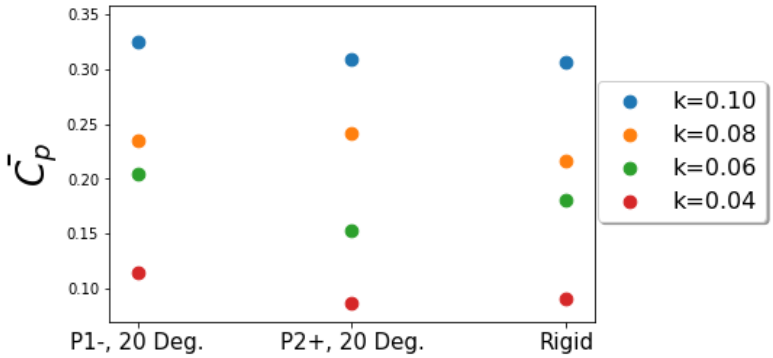

Figure 4.8: Cycle mean heaving power coefficient for rigid case and P1- and P2+ trailing edge motions at a trailing edge amplitude of 20° with reduced frequency k = 0.10, 0.08, 0.06, and 0.04.

4.3 Effect of Reduced Frequency

The final parameter of interest is reduced frequency. This portion of the work entails quantifying the effect of altered reduced frequency upon trailing edge motion performance relative to the rigid case. The two trailing edge motions from the previous section, P1- and P2+, are selected for further investigation, both at an amplitude of 20°. While experiments up until this point were performed strictly at a reduced frequency of $k = 0.08$, these tests cases, as well as the datum rigid case, were performed again at reduced frequencies of $k = 0.10$, $k = 0.06$, and $k = 0.04$. For $k = 0.10$, this entailed increasing the flapping frequency to $f = 1.8$ Hz, and slightly reducing the wind speed, while for the cases of $k = 0.06$ and $k = 0.04$ the flapping frequency of $f = 1.6$ Hz was maintained and the wind speed increased.

For $k = 0.10$, resulting transient coefficients of lift and power are given in Figures 4.9 and 4.10 respectively. Similarly, for $k = 0.06$, curves are given in Figures 4.11 and 4.12. For $k = 0.04$, curves may be found in Figures 4.13 and 4.14. The efficiencies and cycle-averaged coefficients of heaving power for all cases

of adjusted reduced frequency are given in Figures 4.7 and 4.8, respectively.

4.3.1 k = 0.10

When the reduced frequency is increased to k = 0.10, the effect of usage of the P1- trailing edge motion is clearly illustrated in Figure 4.9: A slight increase in magnitude of the primary and secondary lift force peaks is observed, an effect which is accompanied by a slight phase shift in each of their occurrence. However, a subtle increase in the rate at which forces taper off from maximum values counteracts this, yielding a heaving power curve which peaks much higher than that of the rigid case, but which possesses only a marginally better encapsulated area as illustrated in Figure 4.10. As a consequence, the P1- profile demonstrates a 6.0% increase in coefficient of heaving power relative to the rigid case. Further, an efficiency reduction of 1.0% is observed as a consequence of increased swept area.

Similarly, the P2+ motion profile also does not offer a particularly substantial power improvement in this configuration either. As illustrated in Figure 4.9, it manages to closely mirror the performance of the P1- motion during the first half of the cycle. While the primary and secondary peaks are both suppressed relative to P1-, they are also delayed. However, a stark difference is observed during the second half of the cycle - the primary lift force peak becomes much more reduced in magnitude, but broader. This asymmetry is unique to this test case in particular. Consequentially, the behavior of the transient coefficient of power in this case (see Figure 4.10) is very similar to that of the P1- and rigid cases during the first half of the cycle, but much broader during the second half. This is somewhat advantageous, as exerted lift forces experience a slight buff when heaving velocity

is greater. Therefore, during the second half of the cycle, the transient coefficient of power ramps up noticeably more slowly, but remains greater in magnitude later in the half-cycle. Regardless, the cycle-averaged performance metrics demonstrate that P2+ is unable to dramatically improve the performance of the rigid test case either, with measured increases of only 1.1% present in both efficiency and cycle-averaged heaving power coefficient.

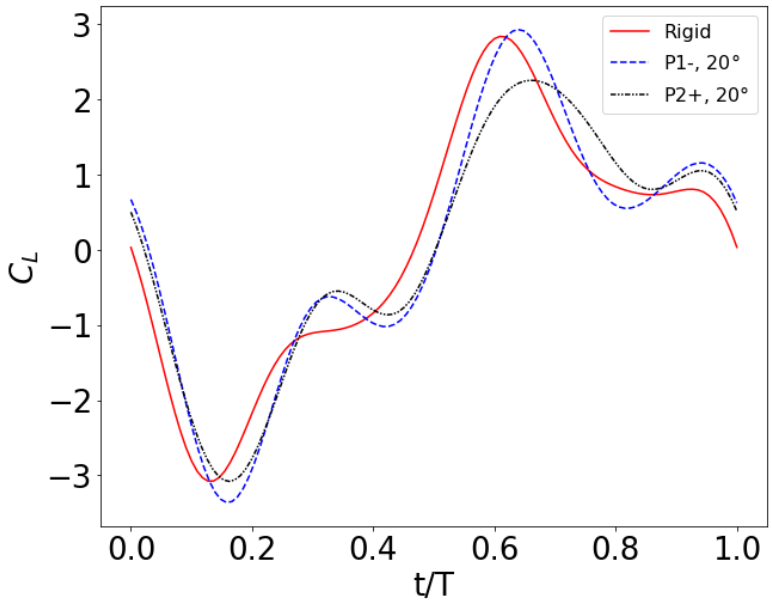

Figure 4.9: Transient coefficients of lift for P1- and P2+ trailing edge motions at a trailing edge amplitude of 20° with reduced frequency k = 0.10. Also shown are rigid case results taken with the same airfoil under the same experimental conditions.

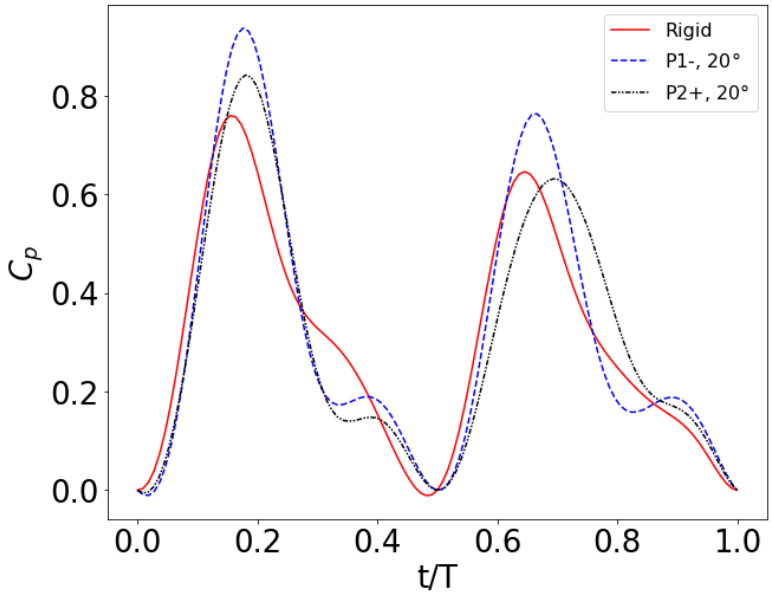

Figure 4.10: Transient coefficients of heaving power for P1- and P2+ trailing edge motions at a trailing edge amplitude of 20° with reduced frequency k = 0.10. Also shown are rigid case results taken with the same airfoil under the same experimental conditions.

4.3.2 k = 0.06

While P1- offers a cycle-averaged heaving power coefficient increase of 6.0% at $k = 0.10$ at the lower amplitude of 20°, that increase becomes 8.8% when the reduced frequency is reduced to $k = 0.08$. When the reduced frequency is reduced to $k = 0.06$, this trend continues and the performance is enhanced again - an increase of 12.6% is observed in the cycle-averaged heaving power coefficient relative to the rigid case.

This is a consequence of observed lift forces as illustrated in Figure 4.11. Predominately, the motion is advantageous during the first half of the cycle, where it

manages to not only delay the primary lift force peak, but enhance it substantially. Interestingly, a small delay in the secondary peak is observed, but no meaningful increase in magnitude. During the second half of the cycle, the secondary peak is delayed so late that it is nearly unrelated to power output of the device. Further, the primary peak, though increased slightly in magnitude, occurs earlier. As is clearly illustrated in Figure 4.12, a massive increase in power extraction capability is present during the first half of the cycle. However, performance during the second half of the cycle is not particularly impacted. Within the present study, this effect appears to be unique to the trailing edge motion operation at a reduced frequency of $k = 0.06$. As illustrated in Figures 4.11 and 4.12, a similar but opposing impact is observed in the P2- test case, indicative of this unique behavior not being an experimental shortcoming confined to a single test case. As a consequence of increased swept area, the 12.6% increase in heaving power measured in the P1- case is accompanied by only a 5.2% efficiency increase over the rigid case at the same reduced frequency.

At the present reduced frequency ($k = 0.06$), the P2+ test case, which performed favorably at $k = 0.08$, becomes a drastic disadvantage. As shown in Figure 4.11, it causes a large reduction in force magnitudes during the first half of the cycle, as well as the presence of an unfavorable phase shift in the primary force peak. During the second half of the cycle, the same effects are present, but less exacerbated. With this is mind, it is unsurprising that Figure 4.12 demonstrates disheartening power extraction capacity relative to the rigid case. A reduction of 15.3% in efficiency and cycle-averaged heaving power coefficient are measured relative to the rigid case.

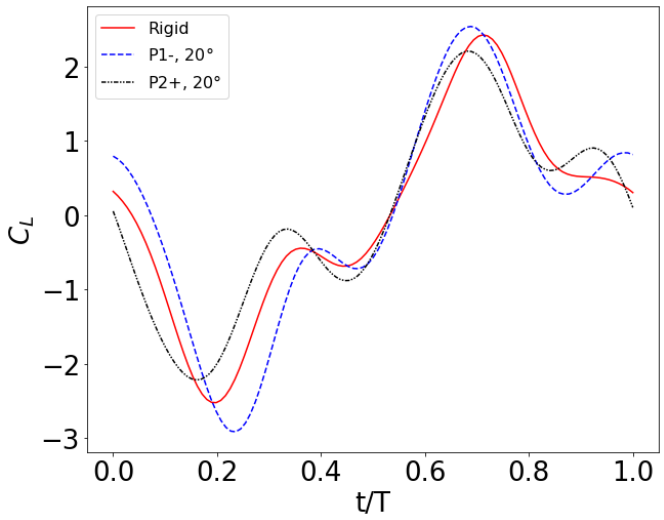

Figure 4.11: Transient coefficients of lift for P1- and P2+ trailing edge motions at a trailing edge amplitude of 20° with reduced frequency k = 0.06. Also shown are rigid case results taken with the same airfoil under the same experimental conditions.

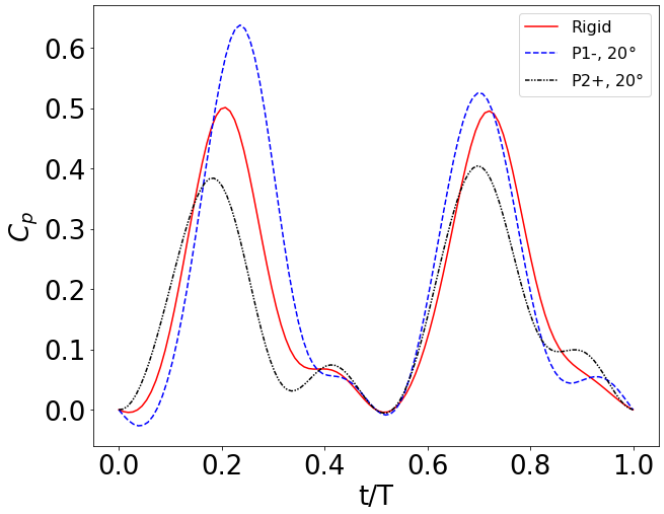

Figure 4.12: Transient coefficients of heaving power for P1- and P2+ trailing edge motions at a trailing edge amplitude of 20° with reduced frequency k = 0.06. Also shown are rigid case results taken with the same airfoil under the same experimental conditions.

4.3.3 k = 0.04

At $k = 0.04$, the improvement trend in the performance increase due to employment of the P1- motion profile continues. Increases of 17.3% and 25.6% are seen in efficiency and cycle-averaged heaving power coefficient relative to the rigid case. At a glance, Figure 4.14 demonstrates that these vastly improved performance metrics can be attributed to much greater maxima peak power output. The increase in the maxima of the transient heaving power coefficient is a staggering nearly 50%. Figure 4.13 clearly demonstrates the cause of this: P1- manages to substantially improve the magnitude of the primary force peak, as well as greatly delay it. At $k = 0.04$, the rigid case primary force peak is shifted toward the beginning of the half cycle. This is highly disadvantageous from a power-extraction standpoint, given that the heaving velocity profile is sinusoidal. Therefore, lift forces near the midpoint of the half cycle are crucial to obtaining optimal power output. Shifting the primary peak to so early in the half-cycle results in a drastic, nonlinear reduction in cycle-averaged power output. Interestingly, as illustrated in Figure 4.13, P1- does not substantially impact the secondary peak behavior. Rather, it is remarkably close to that of the rigid case secondary peak performance, considering how drastic the performance variation between the two cases is. The drastic improvement in the magnitude of the primary peak is less significant during the second half of the cycle, as is its phase shift. Again, it would appear that most of the gains associated with P1- are had during the first half of the cycle.

While performance of the P2+ test case is again worse than the rigid case, less drastic reductions are observed when compared to those at $k = 0.06$. For $k = 0.04$, a reduction of 4.7% in efficiency and cycle-averaged heaving power coefficient is observed over the rigid case. As shown in Figure 4.13, a small, favorable phase shift

in the occurrence of the primary lift force peak is present during both halves of the cycle. However, this occurs at a rather large expense in magnitude. While lift force measurements would make it seem that the former is not nearly enough to make up for the latter, Figure 4.14 clearly demonstrates that the non-linearity of the heaving velocity during the early part of each half-cycle results in just the opposite. Interestingly, it is only the reduction in the secondary peak magnitude which results in any substantially sub-par performance during the first half of the cycle. However, the reduction in lift force magnitude becomes much more drastic during the second half of the cycle, resulting in a more substantial reduction in the primary peak of the heaving power coefficient during the second half of the cycle. However, this is counteracted by the less dramatic tapering off of lift forces between the primary and secondary peaks during the second half-cycle, resulting in a much broader curve and area surprisingly close to that of the rigid case. Therefore, the somewhat surprising reduction of only 4.7% in efficiency and cycle-averaged heaving power coefficient presents a much more intriguing set of results than would be anticipated at first-pass inspection, demonstrating the importance of considerations beyond just maximum force magnitudes.

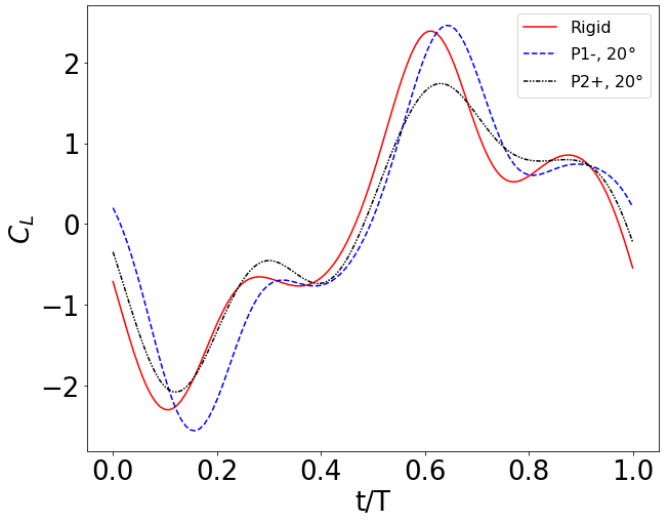

Figure 4.13: Transient coefficients of lift for P1- and P2+ trailing edge motions at a trailing edge amplitude of 20° with reduced frequency k = 0.04. Also shown are rigid case results taken with the same airfoil under the same experimental conditions.

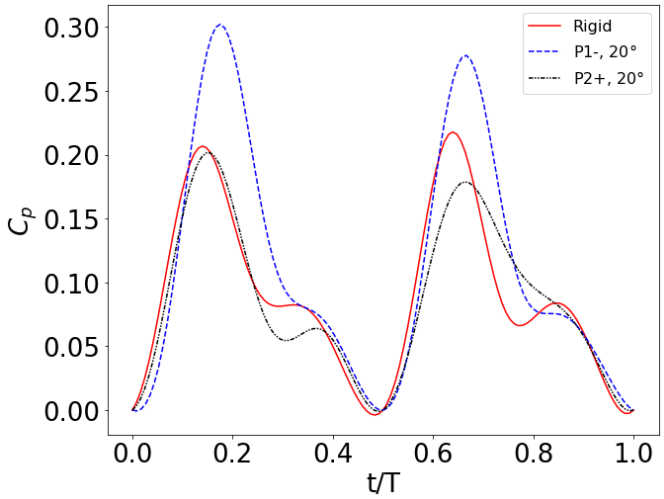

Figure 4.14: Transient coefficients of heaving power for P1- and P2+ trailing edge motions at a trailing edge amplitude of 20° with reduced frequency k = 0.04. Also shown are rigid case results taken with the same airfoil under the same experimental conditions.

Chapter 5: Conclusions

The impact of actively-controlled trailing edge motion upon flapping foils undergoing a kinetic energy harvesting regime has been experimentally studied. Results indicate that reduced trailing edge amplitudes provide better results under the conditions examined. There is a clear impact of trailing edge actuation phase upon the effectiveness of the energy harvesting cycle, both with respect to energy harvesting efficiency and heaving power extraction.

Of the four trailing edge motion profiles initially examined, P1- and P2+ were deemed promising and further studied. Further examination concluded that both were more favorable at a reduced trailing edge amplitude of 20° than the 40° amplitude initially evaluated. Conditionally, the P2+ trailing edge motion profile is more favorable than the rigid case. However, of all motion profiles examined, P1+ at the reduced amplitude of 20° best improves the cycle averaged heaving power coefficient at reduced frequencies of $k = 0.04,\ 0.06$, and 0.10. Further, while P2+ only conditionally offers improvement upon rigid case results, P1- offers an unconditional heaving power extraction improvement of varying magnitude at the reduced trailing edge amplitude under the operational conditions examined.

Perhaps the most intriguing trend illustrated in results is that the increase in cycle averaged heaving power coefficient obtained by the reduced amplitude P1- case over rigid case results increases as reduced frequency is reduced. This trend holds true for $k = 0.08$ and below. This makes an interesting contrast to the results of Siala, which indicate that trailing edge motion does not become advantageous

until greater ($k = 0.17$) reduced frequencies under higher ($0.10 \leq k \leq 0.18$) reduced frequency conditions [9]. Considering these results (which begin at $k = 0.10$) in conjunction with the work presented here (which conclude at $k = 0.10$), it is suggested that trailing edge motion may become disadvantageous in a moderate ($0.10 \leq k \leq 0.17$) reduced frequency regime, but be favorable at both low ($k \leq 0.08$) and high ($k \geq 0.17$) k-values.

Under steady conditions, cambered airfoils experience greater lift forces than comparable symmetric foils. Therefore, it is hypothesized that the actively-controlled trailing edge motion evaluated here can influence the effective camber of the airfoil at key cycle times, resulting in greater lift forces for portions of the cycle. If trailing edge actuation timing and amplitude are carefully selected, this may include the midpoint of each half-cycle, when heaving velocity is maximized. Differences in performance are then associated with an effect had upon the favorable time-variant pressure gradient as a consequence of an influence upon the timing and strength of shed voticies. A future flow visualization study could add a great deal of insight regarding the vortex dynamics responsible for the variation in performance measured in this work.

Bibliography

[1] J Everaert, "Wind turbines and birds in flanders: preliminary study results and recommendations", Natuur.Oriolus **69**, 145–155.

[2] W McKinney and J DeLaurier, "Wingmill: an oscillating-wing windmill", Journal of energy **5**, 109–115 (1981).

[3] X Wu, X Zhang, X Li, and W Lu, "A review on fluid dynamics of flapping foils", Ocean Engineering **195** (2021).

[4] T Kinsey and G Dumas, "Parametric study of an oscillating airfoil in a power-extraction regime", AIAA Journal **46**, 1318–1330 (2008).

[5] FB Tian, J Young, and JC Lai, "Improving power-extraction efficiency of a flapping plate: from passive deformation to active control", Journal of Fluids and Structures **51**, 384–392 (2014).

[6] Q Zhu, "Optimal frequency for flow energy harvesting of a flapping foil", Journal of fluid mechanics **675**, 495–517 (2011).

[7] M Jamil and A Javed, "Design optimization of a semi-active flapping foil in an energy extraction mode", in 2019 international conference on engineering and emerging technologies (iceet) (2019).

[8] D Kim, B Strom, S Mandre, and K Breuer, "Energy harvesting performance and flow structure of an oscillating hydrofoil with finite span", Journal of Fluids and Structures **70**, 314–326 (2017).

[9] FF Siala, K Kamrani Fard, and JA Liburdy, "Experimental study of inertia-based passive flexibility of a heaving and pitching airfoil operating in the energy harvesting regime", Physics of Fluids **32**, 017101 (2020).

[10] MW Prier and JA Liburdy, "Discrete vortex modeling of a flapping foil with activated leading edge motion", in Asme-jsme-ksme 2019 8th joint fluids engineering conference (American Society of Mechanical Engineers Digital Collection, 2019).

[11] AD Totpal, FF Siala, and JA Liburdy, "Energy harvesting of an oscillating foil at low reduced frequencies with rigid and passively deforming leading edge", Journal of Fluids and Structures **82**, 329–342 (2018).

[12] DE Rival, J Kriegseis, P Schaub, A Widmann, and C Tropea, "Characteristic length scales for vortex detachment on plunging profiles with varying leading-edge geometry", Experiments in Fluids **55**, 1660 (2014).

[13] W Liu, Q Xiao, and F Cheng, "A bio-inspired study on tidal energy extraction with flexible flapping wings", Bioinspiration & Biomimetics **8**, 036011 (2013).

[14] J Wu, C Shu, N Zhao, and FB Tian, "Numerical study on the power extraction performance of a flapping foil with a flexible tail", Physics of Fluids **27** (2015).

[15] W Liu, Q Xiao, and Q Zhu, "Passive flexibility effect on oscillating foil energy harvester", AIAA Journal **54**, 1172–1187 (2016).

[16] J Wu, J Wu, FB Tian, N Zhao, and YD Li, "How a flexible tail improves the power extraction efficiency of a semi-activated flapping foil system: a numerical study", Journal of Fluids and Structures **54**, 886–899 (2015).

[17] Z Liu, FB Tian, J Young, and JC Lai, "Flapping foil power generator performance enhanced with a spring-connected tail", Physics of Fluids **29**, 123601 (2017).

[18] B Zhu, Y Huang, and Y Zhang, "Energy harvesting properties of a flapping wing with a adaptive gurney flap", Energy **152**, 117–128 (2018).

[19] P Mancini, A Medina, and AM Jones, "Experimental and analytical investigation into lift prediction on large trailing edge flaps", Physics of Fluids **31**, 013106 (2019).

[20] T Kinsey and G Dumas, "Parametric study of an oscillating airfoil in power extraction regime", in 24th applied aerodynamics conference (2006).

[21] K Lindsey, "A feasibility study of oscillating-wing power generators", MA thesis (Naval Postgraduate School, 2002).

[22] G Peyne, *How to calculate naca 4- and 5- digit sections<-here it is!*, https://web.archive.org/web/20090427002114/http://www.fges.demon.co.uk/cfd/naca.html#07.

[23] Z Liu, KS Bhattacharjee, FB Tian, J Young, T Ray, and JCS Lai, "Kinematic optimization of a flapping foil power generator using a multi-fidelity evolutionary algorithm", Renewable Energy **132**, 543–557 (2019).

[24] L Duarte, N Dellinger, G Dellinger, and A Ghenaim, "Experimental optimization of the pitching structural parameters of a fully passive flapping foil turbine", Renewable Energy **171**, 1436–1444 (2021).

[25] J Deng, C Caulfield, and X Shao, "Effect of aspect ratio on the energy extraction efficiency of three-dimensional flapping foils", Physics of Fluids **26**, 043102 (2014).

[26] A Totpal, "The energy extraction performance of an oscillating rigid and flexible foil", MA thesis (Oregon State University, 2017).

[27] V Ngo, "Leading edge separation analysis of oscillating airfoil energy harvesters", MA thesis (Oregon State University, 2021).